On-Chip Active Control of Ultra-High-*Q* Terahertz Photonic Topological Cavities

Abhishek Kumar[1,2†], Manoj Gupta[1,2 †], Prakash Pitchappa[3], Thomas Caiwei Tan[1,2], Udvas Chattopadhyay[1], Guillaume Ducournau[4], Nan Wang[3], Yidong Chong[1,2], Ranjan Singh[1,2 *]

[1]Division of Physics and Applied Physics, School of Physical and Mathematical Sciences, Nanyang Technological University, Singapore 637371
[2]Center for Disruptive Photonic Technologies, The Photonics Institute, Nanyang Technological University, Singapore 639798
[3]Institute of Microelectronics, Agency for Science, Technology and Research, 2 Fusionopolis Way, Singapore 138634

[4]Institut d'Electronique de Microelectronique et de Nanotechnologie (IEMN), UMR CNRS 8520, Universite de Lille 1,59652 Villeneuve d'Ascq CEDEX, France

** Corresponding Author- ranjans@ntu.edu.sg*

† The authors contributed equally

Abstract

Rapid scaling of semiconductor devices has led to an increase in the number of processor cores and integrated functionalities onto a single chip to support the growing demands of high-speed and large-volume consumer electronics. To meet this burgeoning demand require an improved interconnect capacities in terms of bandwidth density and active tunability for enhanced throughput and energy efficiency. Low-loss terahertz silicon interconnects with larger bandwidth offers a solution for existing inter/intra chip bandwidth density and energy efficiency bottleneck. Here, we present a low-loss terahertz topological interconnect-cavity system that can actively route signals through sharp bends, by critically coupling to a topological cavity with an ultra-high-quality (Q) factor of 0.2×10^6. The topologically protected large Q factor cavity enables energy-efficient optical control showing 50 dB modulation. We further demonstrate the dynamic control of the critical coupling between the topological interconnect-cavity for on-chip active tailoring of the cavity resonance linewidth, frequency, and modulation through complete suppression of the back reflections. The on-chip topological cavity is CMOS-compatible and highly desirable for hybrid electronic-photonic

This article has been accepted for publication and undergone full peer review but has not been through the copyediting, typesetting, pagination and proofreading process, which may lead to differences between this version and the Version of Record. Please cite this article as doi: 10.1002/adma.202202370.

technologies for sixth (6G) generation terahertz communication devices. Ultra-high-*Q* cavity also paves the path for designing topological lasers, quantum circuits, and nonlinear topological photonics.

Introduction

The global digitalization and the rapid rise of artificial intelligence (AI) and cloud-based services have led to an ever-increasing demand for higher data transfer rates in wired and wireless communication links. The exponential growth in data rates has pushed the carrier frequencies towards the higher spectral region, terahertz (THz) bands. In fact, the availability of ultra-high bandwidths in the THz region (0.1-10 THz) allows to achieve terabits per second connectivity[1], making it ideal for the next generation communication: 6G communication. However, with the emergence of 6G networks, the development of an efficient on-chip communication with low loss and active control is crucial to handle and process the massive volume of data transmitted using THz carrier frequencies. The existing solutions for high-speed on-chip interconnects, including copper-based electrical interconnects (EIs)[2] suffer from limited bandwidth, and optical interconnects (OIs)[3] possesses integration complexity and electronic-to-optical (EO/OE) conversion losses. To circumvent the existing performance gaps (in terms of bandwidths, energy efficiency and system's simplicity) of on-chip interconnects, *THz interconnects* [4,5] offers a potential route by leveraging the advantages of both the electronic and photonic worlds. However, scaling carrier frequencies up to sub-THz and beyond requires further innovation towards on-chip photonic solutions to support higher radio frequency (RF) electronics that have limited power amplification capabilities at the THz regime.[6] In addition, there is increasing demand for active on-chip terahertz photonic devices with negligible losses that could be heterogeneously integrated with RF CMOS electronics[6]. Thus far, integrated THz photonic solutions have been limited to passive interconnects[7–10] and routing[11]. Integrated photonic circuits

typically suffer losses due to the back-reflection of guided waves. This leads to cross talk (noise) in inter/intra channel, which becomes more significant as the level of integration increases with more functional devices such as splitters, resonators and multiplexers connected on a single chip. In this context, the recently discovered Photonic Topological Insulators (PTIs)[12–15] offer a possible solution. PTIs are photonic structures that support edge states at the interface between two domains with topologically distinct photonic band structures. These edge states can be designed to be robust against back reflections even at sharp bends, corners, and lattice defects. Photonic topological edge states have already enabled a variety of novel photonic devices, such as reflectionless waveguides[15], robust delay lines[16], spin-polarized switches[17], non-reciprocal devices[15,18], topological splitters[17] and lasers[19,20]. However, the exploration of PTI devices is largely limited to optical or microwave regime. PTI in the THz spectral range can be excellent candidates for information carriers, owing to its single-mode and linear dispersion characteristics, advantageous for on-chip THz communication. More importantly, achieving active control in the PTI platform opens a new dimension for THz wave manipulation, which is critical for developing efficient chip-scale reconfigurable THz devices. Recent efforts to dynamically tune the photonic topological edge states have involved the integration of liquid crystals[21], Kerr nonlinearities[22], photo-excitation[23] and phase change materials[24]. However, these experimental demonstrations are limited to microwave and optical frequencies. It is challenging to translate these approaches into the THz regime, owing to weak nonlinearities and incompatibility with on-chip designs.

Here, we design and demonstrate an active topological interconnect-cavity integrated chip with an ultra-high quality factor (Q = 0.2 x 10^6) resonance in a topologically protected terahertz cavity based on a Valley Photonic Crystal (VPC)[25], a photonic analogue of 2D valleytronic materials[26]. VPCs host topologically protected valley-locked edge states in

compact structures with wavelength-scale periodicity[25,27], without the need for external magnetic fields or complex fabrication requirements, and are thus highly suitable for implementing photonic chips. The demonstration of the topological cavity-waveguide integration on the CMOS-compatible all-silicon (Si) platform will serve as the fundamental building block for realizing advanced functional THz devices such as on-chip filters, loss-less routers, efficient modulators, and multiplexers. We experimentally demonstrate low power, all-optical control of topologically protected THz waves in the topological cavity-waveguide chip, as shown schematically in Figure 1. The topological cavity, composed of a VPC waveguide closed loop (see Figure 1), exhibits a quality factor (Q) of 0.2×10^6, the first experimental demonstration of such an ultra-high-Q resonance at the THz frequencies. Upon photoexcitation of the topological cavity with a continuous laser of wavelength 532 nm (above the bandgap of Si), we demonstrate a nearly 50 dB modulation of the cavity resonance at an operating frequency of 330 GHz. We also show that critical coupling between the topological cavity and VPC waveguide can be actively tuned by controlling the cavity decay rate through low-power photoexcitation (~ 550 μW) along the VPC domain wall loop that forms the cavity. In addition, off-domain-wall photoexcitation at high pump powers allows the cavity resonance frequency to be tuned by up to 1 GHz, enabling frequency-agile operation of THz resonant modulation. The VPC platform can serve as the basis for developing robust, compact and multifunctional integrated THz devices for the 6G communication and creates an avenue for exploring various fundamental phenomena such as low threshold topological lasing[19,20,28], photon-phonon interactions[29,30], and nonlinear topological effects[31].

Results and discussion

We designed and fabricated a VPC cavity-waveguide chip on high resistive silicon (HR-Si) wafer with a resistivity of 10 kΩ-cm. The HR-Si offers a low loss, high refractive index (~

3.42)[32] and CMOS compatible platform for implementing integrated THz devices. Figure 1 shows the artistic illustration of VPC cavity-waveguide functionality achieved upon photoexcitation of the topological cavity. In Figure1a, the black and grey highlighted regions indicate the topologically distinct VPC domains formed by Type A and Type B unit cells, respectively. The sign of $\delta = l_2 - l_1$ differentiates Type A ($\delta > 0$) and Type B ($\delta < 0$) unit cells, which gives rise to opposite valley Chern numbers and therefore belongs to different topological phases, as highlighted in Figure1a, and discussed in detail in Figure 2. The interface of Type A and Type B unit cells hosts valley-polarized topological edge states, also known as kink states. To highlight the robustness of the kink states, we designed an "Ω-shaped" topological waveguide consisting of a VPC domain wall with four sharp corners, as indicated by the yellow line in Figure 1a. An adiabatically tapered coupler was designed to couple incoming THz waves to kink states in the VPC waveguide with minimal impedance mismatch. We constructed the topological cavity by forming a closed-loop domain wall between $\delta > 0$ (black colored unit cell) and $\delta < 0$ (grey colored unit cell) VPC domains, as indicated by the orange line in Figure 1a. The loop hosts kink states at discrete eigenfrequencies, analogous to whispering gallery modes (WGMs)[33]. Despite the sharp corners in the loop, the kink states circulate with minimal counter-propagation, resisting the formation of standing waves, hence giving rise to a series of regularly spaced resonances (see supplementary information, section S2). The topological cavity is fundamentally different from traditional cavity designs such as photonic crystal cavities[34–36] or nanobeam cavities[37], which rely on careful structural optimization. The geometrical insensitivity of the topological cavity offers excellent flexibility in design and fabrication; although we have focused on a parallelogram-shaped loop with four sharp corners, it is possible to design cavities with other shapes (see Supplementary information, section S2).

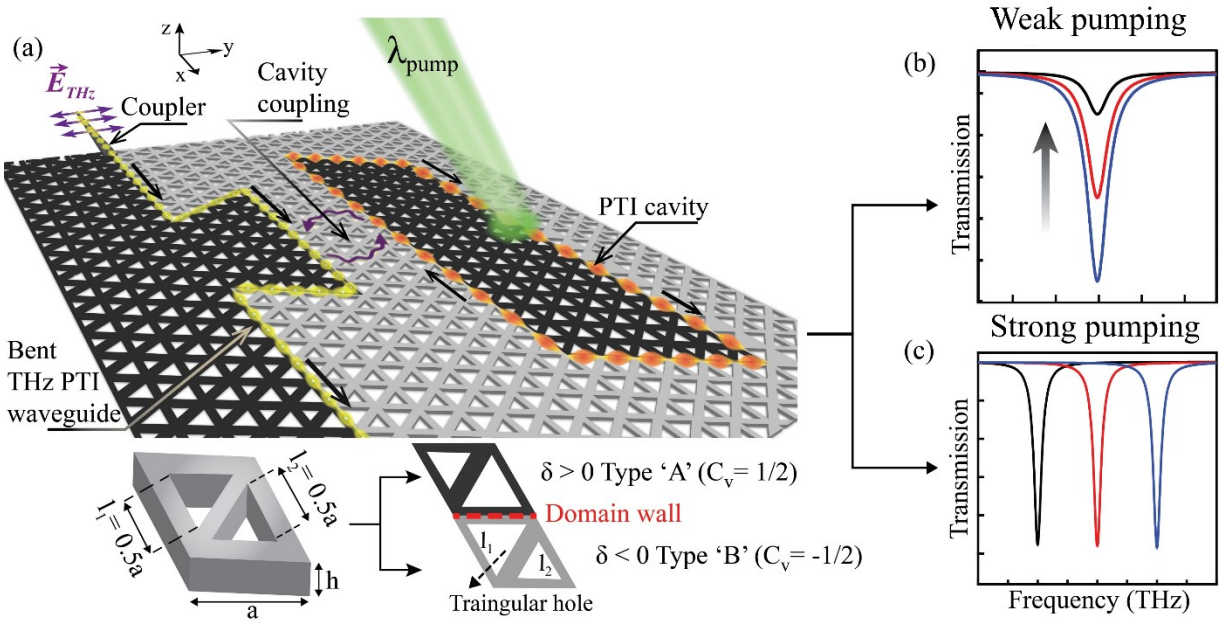

Figure 1 All-optical control of a terahertz topological cavity-waveguide chip. a, Artistic illustration of a VPC cavity-waveguide in an all-silicon (Si) platform. A continuous laser with wavelength 532 nm (energy 2.33 eV) photoexcites the Si above the bandgap (1.1 eV). Inset shows the unit cell of the VPC, where *a* denotes the periodicity and *h* represents the height equal to 200 μm. The unit cell contains two triangular air holes of side lengths l_1 and l_2. For symmetric structure, $l_1 = l_2 = 0.5a$. $\delta = l_2 - l_1$ denotes the degree of asymmetry, with $\delta > 0$ and $\delta < 0$ corresponding to Type A and Type B VPCs (respectively shaded in black and grey in the schematic). **b,** Schematic illustration of THz intensity modulation caused by photoexciting the domain wall of VPC cavity. **c,** Schematic representation of frequency agility of the topological cavity resonance upon high-power photoexcitation.

Here, we focus on transverse electric (TE) modes, for which the electric fields are confined in the *xy* plane. The thickness (*h*) of the silicon membrane is 200 μm, ensuring vertical confinement (*z*-direction) via total internal reflection[7,38]. The VPC structure consists of a hexagonal lattice of lattice constant a = 242.5 μm, with each unit cell containing two equilateral triangular holes of side length l_1 and l_2 (inset of Figure 1a). When both triangular holes have the same size ($l_1 = l_2 = 0.5a$), the photonic crystal possesses C_6 symmetry, and its band structure exhibits gapless Dirac points at K/K' as shown in Figure 2a. By setting the sizes of the triangular holes to be unequal (l_1 = 0.65a and l_2 = 0.35a), we break the inversion symmetry and lift the degeneracies of the Dirac points, opening a topological bandgap (320-

350 GHz) (Figure 2a). Each of the two valleys (around K and K') carries nonzero and opposite signed Berry curvature (an abstract "magnetic field" in the momentum space). To highlight this, we numerically calculated the Berry curvature for Type A and Type B unit cells over the entire Brillouin zone. The results are shown in Figure 2b, where we observe that for Type A (Type B), the peak of Berry curvature is mainly localized around K'(K) valley while the sink is around K(K') valley. Since the VPC preserves the time-reversal (TR) symmetry, integrating the Berry curvature over the entire Brillouin zone leads to zero Chern number. Hence, to characterize the valley-Hall phase, a topological invariant called valley Chern number is defined, whose definition is similar to Chern number except the integrating of Berry curvature is performed near to the valleys[25,39]. For a given type of unit cell (Type A or Type B) the sign of valley Chern number is opposite at each K and K' valleys. And, for a given valley, the valley Chern number is complementary for Type A and Type B unit cells. Consequently, interfacing both the unit cells leads to valley-dependent topological kink states which are robust even at sharp corners or defects unless the intervalley mixing is absent.

Further, inspecting the Bloch states of Type A and Type B unit cells at nonequivalent K/K' valleys reveals that the Bloch states are self-rotating in phase, shown in Figure 2c. This is analogous to the valley-dependent orbital magnetic moments of electrons[39,40]. Figure 2c depicts that the self-rotation of Bloch states at K and K' valleys are in opposite directions. The chirality of phase vortex in Type A and Type B unit cells at K/K' valleys ensure selective coupling of kink states at AB and BA interfaces and prevent intervalley mixing in our topological cavity-waveguide chip (see supplementary information, section S3). According to bulk boundary correspondence, a pair of valley-polarized kink states lock to K and K' valleys with opposite group velocities appear at AB and BA interface within the bandgap. The simulated projected band diagram shown in Figure 2d is consistent with this, where we calculated the dispersion of kink states in the bandgap. The dashed black line

depicts the light line which indicates the dispersion of air, and the grey shaded area highlights the leaky region. It should be noted that not all types of domain walls support kink states; for example, armchair interfaces do not support such states due to the existence of strong intervalley mixing[25,41]. We focus on zigzag-type interfaces, which preserves the valley pseudospin and supports robust kink states.

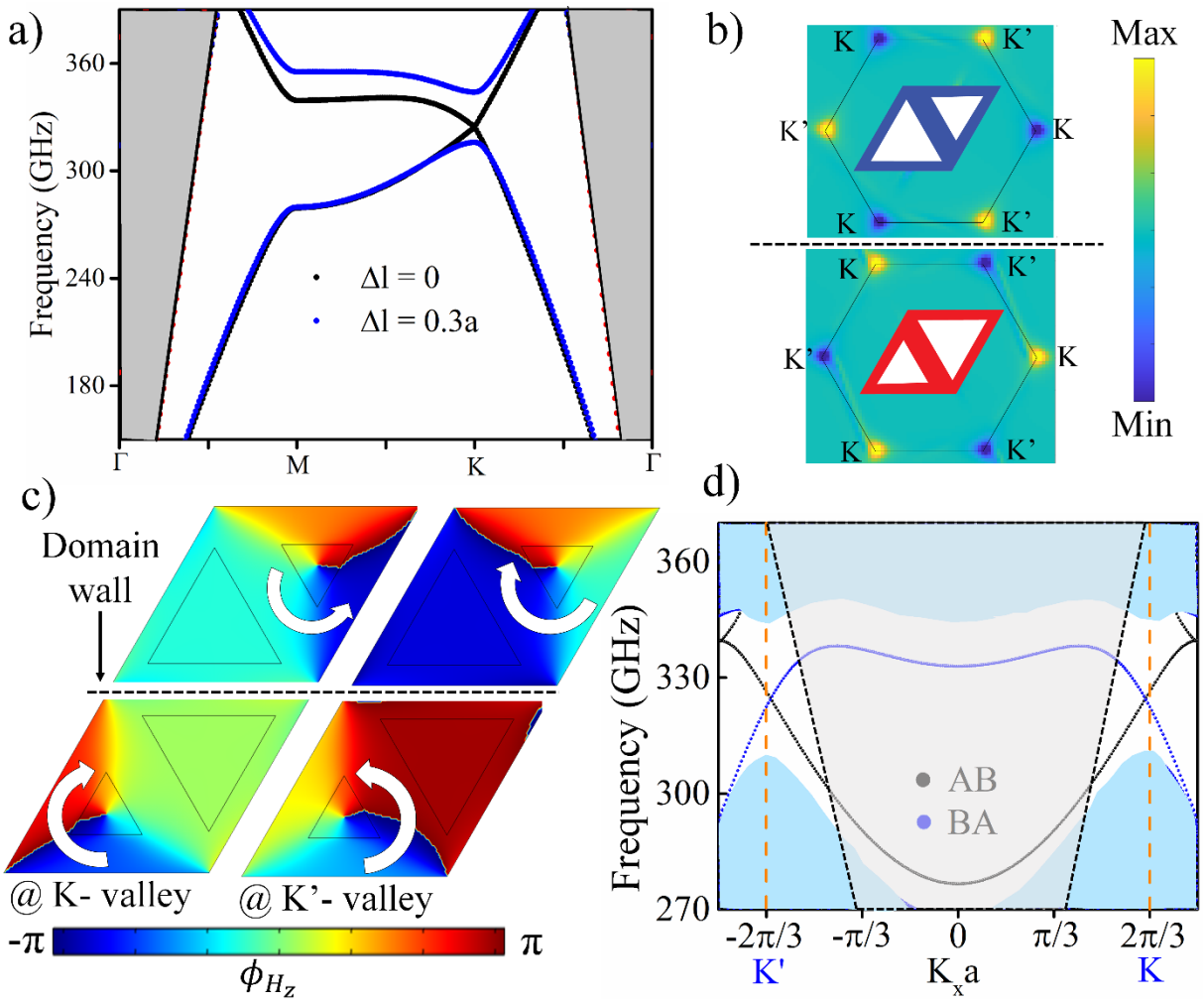

Figure 2 Topological valley photonic crystal (VPC). a, Band diagram with (blue dots) and without (black) inversion symmetry breaking. Here, $\Delta l = l_1 - l_2$. The grey area represents above the light line region. **b**, Distribution of Berry curvature for Type A (top) and Type B (bottom) unit cells. The Berry curvature is localized near to K and K' valleys. **c,** Phase distribution for *z*- oriented magnetic field H_z for Type A and Type B unit cell at K and K' valleys. The phase rotation inside the unit cells is opposite to each other at K and K' valleys. **d**. Dispersion of topological kink states for AB and BA interface. The blue region highlights the projected bulk dispersion. The black dashed light shows the light line. Black and blue dots show the dispersion of kink state at AB and BA interface, respectively. K_x denotes the wavevector along the domain wall, and "*a*" is the lattice periodicity.

To experimentally demonstrate the robust on-chip propagation of THz waves, we measured the transmission spectra from the topological cavity-waveguide chip. The transmission is measured using an electronics-based continuous-wave THz spectrometer. Figure 3a shows the schematic of the experimental setup where the incoming THz waves are coupled to the topological cavity-waveguide chip through an input coupler and an output coupler is utilized to receive the signal at the receiver end. The readers are directed to the method section for a detailed discussion of the experimental setup. Figure 3b shows the experimentally recorded transmission spectrum. Here, we observe sharp dips corresponding to the eigenfrequencies of the topological cavity. The measured loaded Q factors for these resonances are $Q_1 = 0.2 \times 10^6$ and $Q_2 = 0.15 \times 10^5$, corresponding to linewidths of 1.6 MHz and 22 MHz (see Supplementary Information, Section S2 and S4). The differences in the loaded Q factor arise due to different radiative and coupling losses of each resonant mode. These are the highest Q factors measured in THz cavities (see Table 1) and the narrowest measured resonance linewidth of 1.6 MHz at THz frequencies. The robustness of valley kink states against the sharp corners and structural defects ensures the circulation of topological cavity modes with minimal counter-propagation, resisting the formation of standing waves that yields regularly spaced resonance modes (see section S2). In addition, the reflection-free transport of valley kink states in our topological cavity-waveguide chip significantly reduces the coupling loss by eliminating the reflection path, which is impossible in the conventional photonic cavities[35–37]. The strong resilience of valley kink states combined with a low-loss Si platform leads to the ultra-high loaded Q factor in the topological cavity-waveguide chip.

The deep transmission dips observed in Figure 3b imply that the THz waves incident along the topological waveguide at the resonance frequencies are almost entirely dissipated by the topological cavity. By further fine-tuning, the cavity's intrinsic loss rate relative to the waveguide-cavity coupling rate, the absorption at resonance can be tailored to approach

100%, a condition known as "critical coupling"[42]. Critically coupled photonic circuits have been shown to be useful for high-speed light switching, amplification and modulation[43]. Using topologically protected photonic modes to achieve critical coupling is advantageous as reflection can be suppressed entirely compared to conventional photonic circuits. This reduces the crosstalk from other functional components such as splitters, sources, resonators, and multiplexers.

Furthermore, the attainment of critical coupling leads to enhanced transmission at the topological cavity resonance frequency (see Figure 3d). Therefore, achieving an active way to bring the system into the critical coupling regime is vital for developing on-chip topological and conventional cavity-based modulators and switches[44]. Our present system can be actively tuned towards (or away from) the critical coupling by photoexcitation to control the intensity of the resonant transmission dips.

To demonstrate active modulation, we photoexcite the domain wall of the topological cavity with a continuous laser of wavelength 532 nm (above the bandgap of silicon, 1.1 eV) at low pump power ~ 550 μW. Photoexciting the silicon above the bandgap generates free carriers, altering the cavity's intrinsic loss rate. We define the absorption enhancement factor $\Delta A = A_{pump} - A_{passive}$, where A_{pump} and $A_{passive}$ represent the strength of the cavity resonances (the intensity of the dip in the transmission spectrum) with and without photoexcitation, respectively. Figure 3c shows the experimentally recorded transmission spectra at various optical pump power, where the transmission dip is significant for 0.55 mW. Further to validate this, in Figure 3d we plot the experimentally obtained graph of ΔA versus optical pump power, which peaks at 550 μW photoexcitation power. This represents the critical coupling point that manifests as enhanced transmission dip at the topological cavity's resonance frequency.

By further increasing the optical pump power, the free carrier density and hence the loss rate increases, driving the system from critical coupling to under-coupling (or over-damping). In this regime, the transmission dips are shallower than in the passive system, corresponding to negative values of ΔA. This behavior is observed in the experimentally obtained transmission curves plotted in Figure 3c. The under-coupled regime can be exploited to achieve large modulation of transmission. Using the same 532 nm continuous laser and illumination spot, we increase the pump power from 550 μW up to 40 mW. The resulting transmission spectra, shown in Figure 3c, exhibit nearly 50 dB of resonance modulation over the tested range of photoexcitation pump powers.

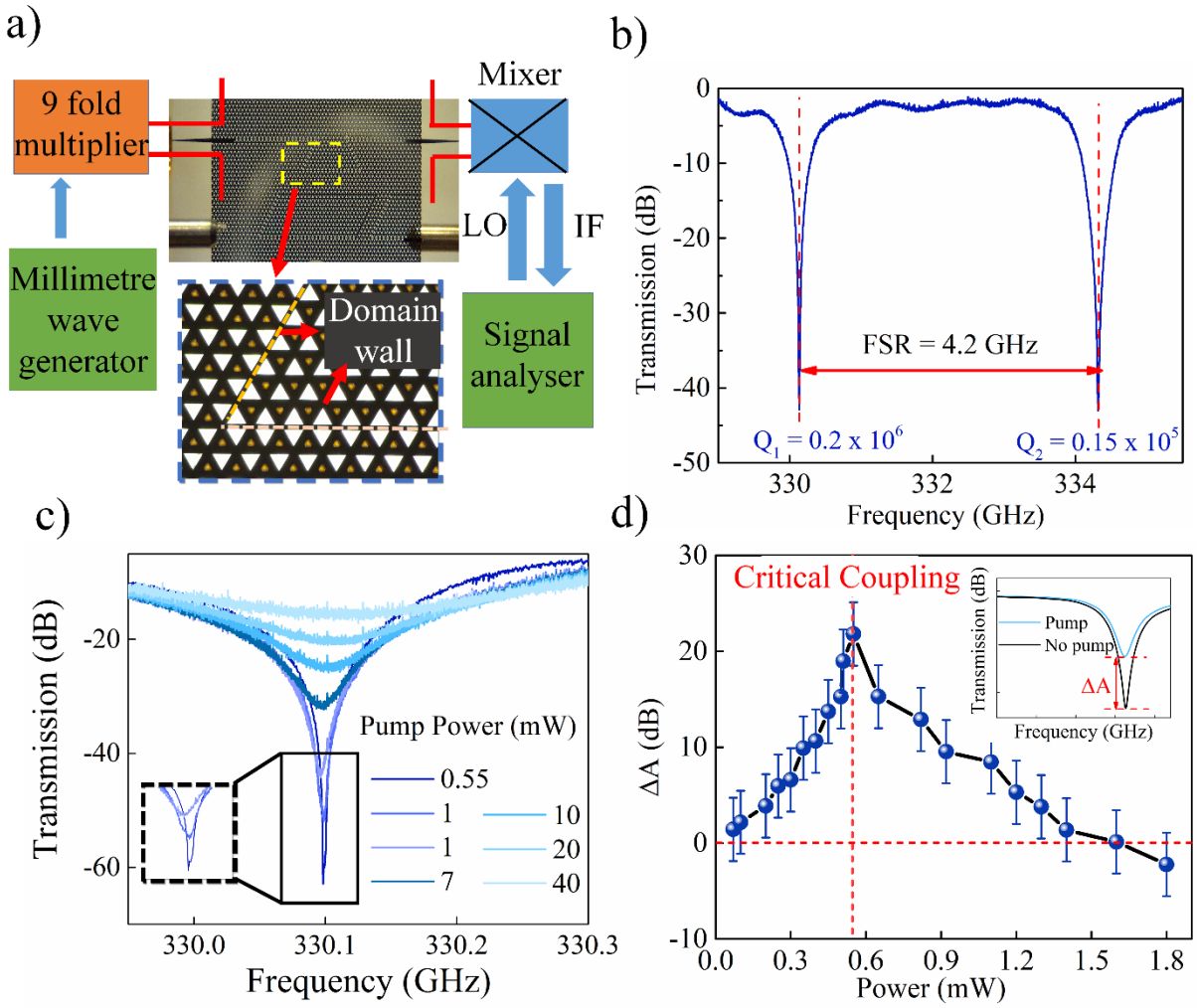

Figure 3 Experimental characterization of topological cavity-waveguide chip a, Schematic of experimental setup to measure transmission spectrum. The detailed discussion of the experimental setup is given in the method section. **b,** Measured transmission spectrum between the input and output ports. The experimental FSR (~ 4.2 GHz) accurately matches the eigenfrequencies analysis (section S2). **c,** Intensity modulation of cavity resonance enabled by photoexciting the domain wall of the topological cavity with a continuous laser of wavelength 532 nm above the bandgap of silicon. At 0.55 mW pump power, the system is close to critical coupling, and the transmission spectrum has a ~ 60 dB dip (solid blue line). The dip becomes shallower with increasing pump power as the system moves further into the under-coupled regime. Inset shows the zoomed portion of the transmission curve to illustrate the intensity modulation clearly. **d,** Experimentally obtained enhancement in cavity absorption versus optical pump power. The enhancement is defined as $\Delta A = A_{pump} - A_{passive}$, where A_{pump} and $A_{passive}$ are strengths (dips in the transmission spectra) at resonance with and without photoexcitation, respectively. The vertical dotted line indicates the point where ΔA is maximum, and the system is closest to the critical coupling condition. Further increasing the optical pump power drives the system to an under-coupled regime with negative ΔA (the horizontal dotted line indicates $\Delta A = 0$). The inset illustrates the pictorial representation of ΔA

Further, we exploited the sensitivity of THz transmission towards photoexcitation to demonstrate intensity modulation of THz wave in the topological cavity-waveguide chip. As shown schematically in Figure 4a, the modulation is achieved by chopping the laser with a mechanical chopper. A spectrum analyzer was utilized to record the change in the topological cavity's resonance intensity. As shown in Figure 4b, we demonstrate ON-OFF intensity modulation with modulation speed up to 10 kHz (the maximum frequency allowed by the mechanical chopper). In contrast, the slow free carrier relaxation (in the range of μs) in intrinsic single-crystalline silicon[45] limits the modulation speed achieved by photoexcitation. This potentially can be improved to the few picoseconds through ion implantation[46,47] of silicon chips yielding modulation speeds of several hundred gigahertz exceeding the bandwidth densities of the state of the art devices. These results are promising for on-chip modulator and switch applications in the THz 6G communications.

Further, we photoexcite the different parts of the topological cavity while keeping the pump power (~ 10 mW) constant. As shown in Figure 4c, the different photoexcitation locations lead to no change in transmission (within the experimental error limits). This indicates that the cavity modes are homogenously spread over the domain wall of the cavity, which is consistent with several previous reports[28,48].

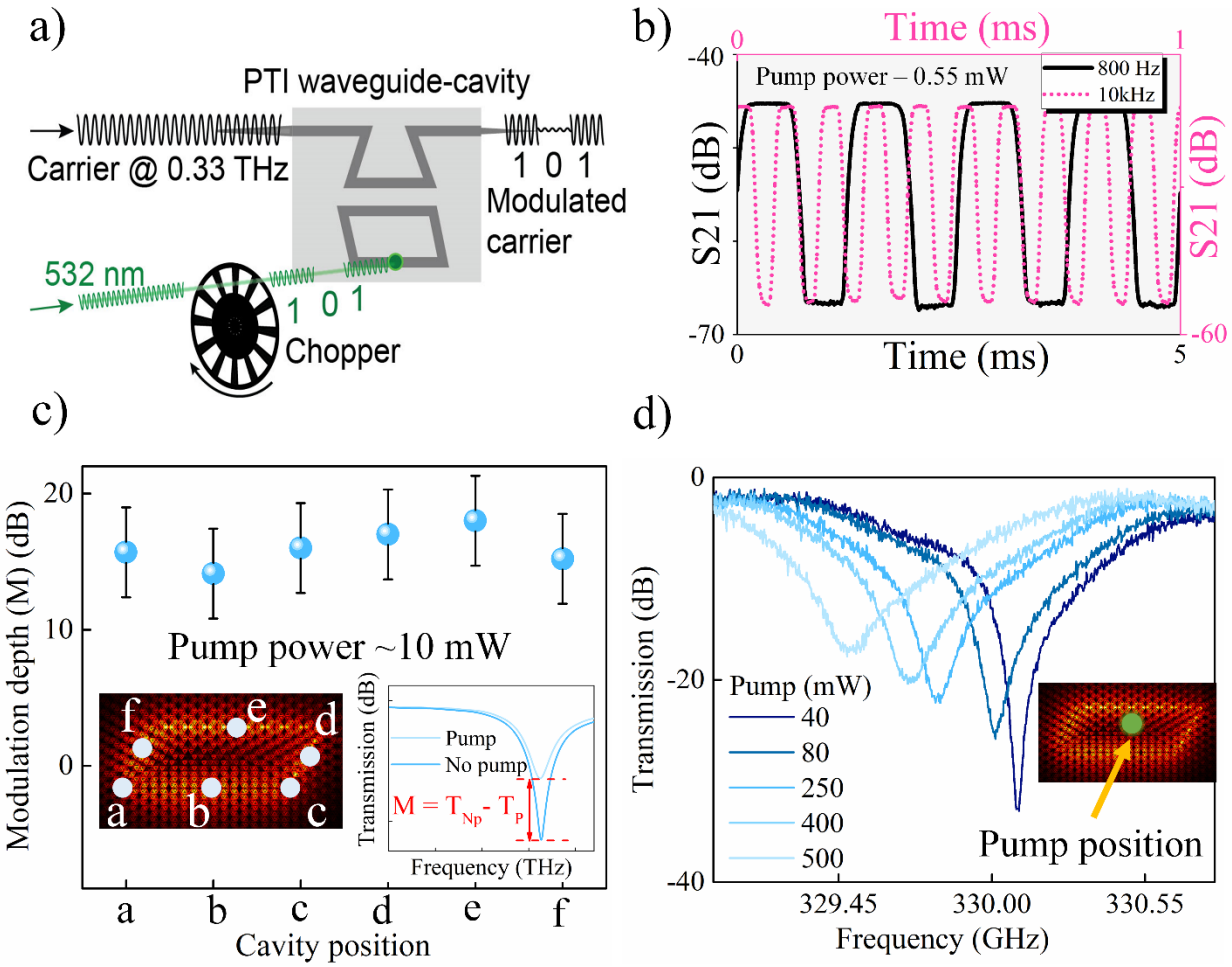

Figure 4 On-chip optical modulation and frequency agility of the topological cavity a, Schematic of the ON-OFF modulation experiment. The setup is similar to Figure 3a, except a mechanical chopper is placed between the laser and the device. The change in the THz wave intensity is recorded by a spectrum analyzer. **b,** Experimentally measured THz wave modulation at different chopper frequencies: 800 Hz (black) and 10 kHz (pink). **c,** Intensity modulation of cavity resonance recorded after photoexciting the topological cavity at various positions marked "a", "b", "c", "d", "e" and "f" (left inset). Right inset shows the change in THz intensity upon photoexcitation. Here, the optical pump power is kept constant at ~ 10 mW. **d,** Transmission spectra at different pump powers, demonstrating tuning of the topological cavity's resonance frequencies by high-power photoexcitation away from the topological cavity's domain wall (inset).

We have also explored a different scheme for modulating the topological cavity, which gives rise to shifts in the cavity resonance frequencies. This is achieved by photoexciting the cavity away from the topological cavity's domain wall (as indicated by the green dot in the inset of

Figure 4d), at higher pump power. Placing the beam spot away from the domain wall avoids quenching of the cavity resonances. Photoexcitation at a high pump power produces a thermal-induced change in the permittivity of the Si , resulting in a redshift of the cavity resonance frequency, given by[49]:

$$\Delta f = -\Delta T \, \frac{f_0}{n_c} \, \frac{dn}{dT} \quad \#(1)$$

where $\frac{dn}{dT}$ is the thermo-optic coefficient of Si with an averaged value of $2.4 \times 10^{-4} \, K^{-1}$[57], f_0 is the resonance frequency, and n_c is the group refractive index. As shown in Figure 4d, over the range of pump powers used in the experiment (40 – 500 mW), we observed ~ 1 GHz of frequency tuning from the baseline resonance frequency (~ 330.11 GHz). To verify that these results are indeed due to the photothermal effect, we heated the cavity with a hot air gun and observed similar frequency shifts, as discussed in detail in Section S7. This scenario can be extremely useful in realizing on-chip THz modulator as spectral tuning of the cavity resonance offers large modulation depth.

In summary, we have experimentally demonstrated extremely high Q resonances in a topological cavity coupled to a topological interconnect as a waveguide in a THz-scale valley photonic crystal implemented on a silicon chip. The Q factors reach up to 0.2×10^6, the highest value reported at THz frequencies. The system is actively tunable, and we demonstrated a variety of photoexcitation schemes for tuning into the critically coupled (60 dB absorption resonance) state, achieving strong optical switching , rapid intensity modulation (20 dB modulation at 10 kHz), and frequency agility (~1 GHz shift in resonance frequency). Active control over topologically protected THz waves in a CMOS-compatible all-Si platform opens new avenues for developing compact and low-loss THz integrated photonic devices. We also envision that such THz chips can be used to explore fundamental

phenomena such as polaritonic interactions[30], low threshold topological lasers[19], topological quantum circuits[50] and nonlinear topological effects[31].

Table 1: Comparison between high *Q* works reported on various platform with our topological cavity-waveguide chip build on all silicon VPC. The reported Q factor is the highest in the THz frequencies.

Scheme	Q factor	Resonance linewidth (MHz)	Frequency (THz)	Topological protection	Chip-integrability	Cavity size*
PC cavity[34,36,51]	10800	~ 28	0.318	No	Yes	~ $0.93\lambda_0$
	11900	~ 8.4	0.1	No	Yes	~ $5.6\lambda_0$
	30000	~ 21	0.632	No	Yes	~ $6\lambda_0$
Racetrack ring[52]	2839	~ 77	0.218	No	Yes	~ $13\lambda_0$
WGM sphere[53]	15000	~ 41	0.62	No	Yes	~ $26\lambda_0$
WGM bubble[54]	440	~ 1000	0.47	No	No	~ $31\lambda_0$
WGM resonator[55,56]	1867-1909	~ 250-260	0.4795	No	Yes	----
	1600	~ 218	0.35	No	-------	~ $21\lambda_0$
Our work (Topological cavity)	**200000**	**~ 1.6**	**0.33**	**Yes**	**Yes**	**~ $20\lambda_0$**

*λ_0 is the corresponding resonance wavelength of the cavity in air.

Methods

Experimental section:

Standard signal generator and spectrum analyzer with frequency extension modules are used to characterize VPC waveguide-cavity device. The microwave frequency through signal generator is upconverted to the desired frequency band (0.26-0.4 THz) by 24-fold frequency-multiplier-module with WR-2.8 hollow waveguide for THz wave output port. The tapered coupler of the sample is used to couple the THz waves from WR-2.8 waveguide. THz transmission through the sample is again outcoupled to signal-analyzer-module through WR-2.8 waveguide to down-convert the incoming signal for spectrum analysis. The signal-analyzer-module upconverts the local oscillator (LO) signal generated from the spectrum analyzer by a factor of 48 and mixes it with incoming THz signal to generate 322.5 MHz intermediate frequency (IF) signal. To obtain the normalized spectra, WR-2.8 waveguides of both modules are first directly connected (without samples) to measure the signal strength in the desired frequency range.

For photoexcitation, a continuous laser of wavelength 532 nm is used. The laser beam is further focused using a convex lens onto the topological cavity-waveguide chip. We kept the beam size small to illuminate only the domain wall of cavity, shown in Supplementary Section S7, Figure S7. For the temporal modulation measurement, a mechanical chopper (Thorlab MC1F10HP) was inserted between the laser and the sample and the change in intensity was recorded by the spectrum analyzer.

Numerical Simulation:

The band structure calculations were performed using a numerical frequency-domain solver (COMSOL Multiphysics), using a parallelogram-shaped unit cell (periodicity 242.5 μm and height 200 μm) containing two equilateral triangular air holes, with Floquet boundary conditions applied in all directions. The detailed simulation results are discussed in Supplementary Information.

Sample Fabrication:

The VPC cavity-waveguide chip was fabricated on an 8-inch diameter high-resistivity silicon (Si) wafer ($\rho > 10$ kΩ/cm). The Si wafer was thoroughly cleaned and 4 μm thick silicon-di-oxide (SiO_2) layer was deposited. Photolithography was used to define the triangular etch holes and device separation trenches. SiO_2 was selectively etched away, exposing the Si surface. Deep reactive ion etching of Si was carried out to etch > 200 μm of Si. The photoresist layer and SiO_2 layers were then completely removed. Back grinding of Si was carried out until 200 μm thick Si was left.

Acknowledgements:

All the authors acknowledge the research funding support from National Research Foundation (NRF) Singapore, Grant No: NRF-CRP-2019-0005.

Author Contributions

A. K. and R. S. conceived the idea of an ultra-high-quality (*Q*) factor topological waveguide cavity and its active control. A. K. designed the topological waveguide-cavity system and performed the simulations. A.K, M.G. and T.C.T carried out the experiments. A.K. performed data analysis with R.S. and Y.C. P.P and N. W. fabricated the silicon device. U.C. performed the numerical calculation for the topological indices. A.K., Y.C. and R.S. wrote the manuscript with inputs from all the authors. R.S planned and led the project.

References

[1] I. F. Akyildiz, J. M. Jornet, C. Han, *Phys. Commun.* **2014**, *12*, 16.
[2] S.-W. Tam, M.-C. F. Chang, J. Kim, G. Byun, in *2011 IEEE Int. Symp. Radio-Freq. Integr. Technol.*, **2011**, pp. 45–48.
[3] A. V. Krishnamoorthy, K. W. Goossen, W. Jan, X. Zheng, R. Ho, G. Li, R. Rozier, F. Liu, D. Patil, J. Lexau, H. Schwetman, D. Feng, M. Asghari, T. Pinguet, J. E. Cunningham, *IEEE J. Sel. Top. Quantum Electron.* **2011**, *17*, 357.
[4] Q. J. Gu, *IEEE Commun. Mag.* **2015**, *53*, 206.
[5] J. W. Holloway, G. C. Dogiamis, R. Han, *IEEE Microw. Mag.* **2020**, *21*, 35.
[6] S. Amakawa, Z. Aslam, J. Buckwater, S. Caputo, A. Chaoub, Y. Chen, Y. Corre, M. Fujishima, Y. Ganghua, S. Gao, J. Grzyb, C. Han, G. JUe, J. Kokkoniemi, Z. Lai, Y. Li, M. Millhaem, I. Moerman, L. Mucchi, S. Myllymäki, R. Nichols, I. Ocket, M. Robertson, M. Rodwell, *ISSN 2669-963X* **2021**.
[7] K. Tsuruda, M. Fujita, T. Nagatsuma, *Opt. Express* **2015**, *23*, 31977.
[8] Y. Yang, Y. Yamagami, X. Yu, P. Pitchappa, J. Webber, B. Zhang, M. Fujita, T. Nagatsuma, R. Singh, *Nat. Photonics* **2020**, *14*, 446.
[9] W. Gao, W. S. L. Lee, X. Yu, M. Fujita, T. Nagatsuma, C. Fumeaux, W. Withayachumnankul, *IEEE Trans. Terahertz Sci. Technol.* **2021**, *11*, 28.
[10] D. Headland, W. Withayachumnankul, X. Yu, M. Fujita, T. Nagatsuma, *J. Light. Technol.* **2020**, *38*, 6853.
[11] M. Yata, M. Fujita, T. Nagatsuma, *Opt. Express* **2016**, *24*, 7835.
[12] T. Ozawa, H. M. Price, A. Amo, N. Goldman, M. Hafezi, L. Lu, M. C. Rechtsman, D. Schuster, J. Simon, O. Zilberberg, I. Carusotto, *Rev. Mod. Phys.* **2019**, *91*, 015006.
[13] A. B. Khanikaev, G. Shvets, *Nat. Photonics* **2017**, *11*, 763.
[14] L. Lu, J. D. Joannopoulos, M. Soljačić, *Nat. Photonics* **2014**, *8*, 821.
[15] Z. Wang, Y. Chong, J. D. Joannopoulos, M. Soljačić, *Nature* **2009**, *461*, 772.
[16] M. Hafezi, E. A. Demler, M. D. Lukin, J. M. Taylor, *Nat. Phys.* **2011**, *7*, 907.
[17] X. Cheng, C. Jouvaud, X. Ni, S. H. Mousavi, A. Z. Genack, A. B. Khanikaev, *Nat. Mater.* **2016**, *15*, 542.
[18] Z. Wang, Y. D. Chong, J. D. Joannopoulos, M. Soljačić, *Phys. Rev. Lett.* **2008**, *100*, 013905.

[19] M. A. Bandres, S. Wittek, G. Harari, M. Parto, J. Ren, M. Segev, D. N. Christodoulides, M. Khajavikhan, *Science* **2018**, *359*, DOI 10.1126/science.aar4005.
[20] B. Bahari, A. Ndao, F. Vallini, A. E. Amili, Y. Fainman, B. Kanté, *Science* **2017**, *358*, 636.
[21] M. I. Shalaev, S. Desnavi, W. Walasik, N. M. Litchinitser, *New J. Phys.* **2018**, *20*, 023040.
[22] D. A. Dobrykh, A. V. Yulin, A. P. Slobozhanyuk, A. N. Poddubny, Yu. S. Kivshar, *Phys. Rev. Lett.* **2018**, *121*, 163901.
[23] M. I. Shalaev, W. Walasik, N. M. Litchinitser, *Optica* **2019**, *6*, 839.
[24] C. Li, X. Hu, W. Gao, Y. Ao, S. Chu, H. Yang, Q. Gong, *Adv. Opt. Mater.* **2018**, *6*, 1701071.
[25] T. Ma, G. Shvets, *New J. Phys.* **2016**, *18*, 025012.
[26] J. R. Schaibley, H. Yu, G. Clark, P. Rivera, J. S. Ross, K. L. Seyler, W. Yao, X. Xu, *Nat. Rev. Mater.* **2016**, *1*, 1.
[27] F. Gao, H. Xue, Z. Yang, K. Lai, Y. Yu, X. Lin, Y. Chong, G. Shvets, B. Zhang, *Nat. Phys.* **2018**, *14*, 140.
[28] Y. Zeng, U. Chattopadhyay, B. Zhu, B. Qiang, J. Li, Y. Jin, L. Li, A. G. Davies, E. H. Linfield, B. Zhang, Y. Chong, Q. J. Wang, *Nature* **2020**, *578*, 246.
[29] S. Mittal, E. A. Goldschmidt, M. Hafezi, *Nature* **2018**, *561*, 502.
[30] S. Barik, A. Karasahin, C. Flower, T. Cai, H. Miyake, W. DeGottardi, M. Hafezi, E. Waks, *Science* **2018**, *359*, 666.
[31] D. Smirnova, D. Leykam, Y. Chong, Y. Kivshar, *Appl. Phys. Rev.* **2020**, *7*, 021306.
[32] J. Dai, J. Zhang, W. Zhang, D. Grischkowsky, *JOSA B* **2004**, *21*, 1379.
[33] K. J. Vahala, *Nature* **2003**, *424*, 839.
[34] E. Akiki, M. Verstuyft, B. Kuyken, B. Walter, M. Faucher, J.-F. Lampin, G. Ducournau, M. Vanwolleghem, *IEEE Trans. Terahertz Sci. Technol.* **2021**, *11*, 42.
[35] Y. Akahane, T. Asano, B.-S. Song, S. Noda, *Opt. Express* **2005**, *13*, 1202.
[36] K. Okamoto, K. Tsuruda, S. Diebold, S. Hisatake, M. Fujita, T. Nagatsuma, *J. Infrared Millim. Terahertz Waves* **2017**, *38*, 1085.
[37] P. B. Deotare, M. W. McCutcheon, I. W. Frank, M. Khan, M. Lončar, *Appl. Phys. Lett.* **2009**, *94*, 121106.
[38] S. Barik, H. Miyake, W. DeGottardi, E. Waks, M. Hafezi, *New J. Phys.* **2016**, *18*, 113013.
[39] X.-D. Chen, F.-L. Zhao, M. Chen, J.-W. Dong, *Phys. Rev. B* **2017**, *96*, 020202.
[40] D. Xiao, W. Yao, Q. Niu, *Phys. Rev. Lett.* **2007**, *99*, 236809.
[41] Y. Ren, Z. Qiao, Q. Niu, *Rep. Prog. Phys.* **2016**, *79*, 066501.
[42] M. Cai, O. Painter, K. J. Vahala, *Phys. Rev. Lett.* **2000**, *85*, 74.
[43] J. M. Choi, R. K. Lee, A. Yariv, *Opt. Lett.* **2001**, *26*, 1236.
[44] A. Yariv, *IEEE Photonics Technol. Lett.* **2002**, *14*, 483.
[45] T. Nozokido, H. Minamide, K. Mizuno, *Electron. Commun. Jpn. Part II Electron.* **1997**, *80*, 1.
[46] A. Chin, K. Y. Lee, B. C. Lin, S. Horng, *Appl. Phys. Lett.* **1996**, *69*, 653.
[47] P. Pitchappa, A. Kumar, H. Liang, S. Prakash, N. Wang, A. A. Bettiol, T. Venkatesan, C. Lee, R. Singh, *Adv. Opt. Mater.* **2020**, *8*, 2000101.
[48] S. Barik, A. Karasahin, S. Mittal, E. Waks, M. Hafezi, *Phys. Rev. B* **2020**, *101*, 205303.
[49] M. W. Pruessner, T. H. Stievater, M. S. Ferraro, W. S. Rabinovich, *Opt. Express* **2007**, *15*, 7557.
[50] Y. Chen, X.-T. He, Y.-J. Cheng, H.-Y. Qiu, L.-T. Feng, M. Zhang, D.-X. Dai, G.-C. Guo, J.-W. Dong, X.-F. Ren, *Phys. Rev. Lett.* **2021**, *126*, 230503.

[51] S. M. Hanham, M. M. Ahmad, S. Lucyszyn, N. Klein, *IEEE Trans. Terahertz Sci. Technol.* **2017**, *7*, 199.
[52] J. Xie, X. Zhu, X. Zang, Q. Cheng, L. Chen, Y. Zhu, *Opt. Mater. Express* **2018**, *8*, 50.
[53] D. W. Vogt, R. Leonhardt, *APL Photonics* **2018**, *3*, 051702.
[54] D. W. Vogt, R. Leonhardt, *Optica* **2017**, *4*, 809.
[55] Z. Wang, G. Dong, S. Yuan, L. Chen, X. Wu, X. Wu, X. Zhang, X. Zhang, *Opt. Lett.* **2019**, *44*, 4670.
[56] D. W. Vogt, R. Leonhardt, *Opt. Lett.* **2017**, *42*, 4359.
[57] M. T. Tinker, J.-B. Lee, *Opt. Express* **2005**, *13*, 7174.

A low-loss terahertz (THz) silicon topological interconnect-cavity system that can actively route signals through sharp bends by critically coupling to a topological cavity with an ultra-high-quality (Q) factor of 0.2×10^6 is shown. We demonstrate on-chip active tailoring of the cavity resonance linewidth, frequency, and modulation at extremely low power through complete suppression of the back reflections, essential for sixth (6G) generation communication with THz topological integrated photonic circuits.